A Low-Power, Ambiguous Synthetic Aperture Radar Concept for Continuous Ship Monitoring

Nertjana Ustalli, Gerhard Krieger, *Fellow, IEEE,* and Michelangelo Villano, *Senior Member, IEEE*

***Abstract*—This paper addresses the design of a low-cost synthetic aperture radar (SAR) for a single dedicated application, namely illegal vessel detection, which can be implemented using a small satellite and is characterized by reduced transmit power and high resolution. Minimum requirements in terms of noise-equivalent sigma zero and resolution that ensure acceptable detection performance are derived based on ship statistics extracted from TerraSAR-X data. One peculiarity of the design is that a pulse repetition frequency much smaller than the nominal Doppler bandwidth is selected to increase the swath width beyond the classical SAR limitation without using digital beamforming, as azimuth ambiguities can be tolerated for this specific application. Several design examples of SAR systems operating in X band demonstrate the potential of this concept for small ship monitoring over swaths of 50-90 km with antennas smaller than 0.6 m^2 and very low average transmit powers comprised between 20 and 80 W.**

***Index Terms*— Azimuth ambiguities, high-resolution wide-swath imaging, ship detection, small satellites, synthetic aperture radar (SAR).**

I. Introduction

Synthetic aperture radar (SAR) systems provide high-resolution, two-dimensional images independently from daylight, cloud coverage, and weather conditions, and are ideal to monitor dynamic processes on the Earth surface in a reliable, continuous, and global way [1].

In order to cope with the demand for high image quality, most state-of-the-art SAR systems are sophisticated and costly with large antennas onboard of heavy spacecrafts [2]. On the other hand, small satellites have been developed in recent years with the goal to address Earth observation applications in a rapid and affordable manner. The global space industry is thus rapidly changing, with the rise of a large number of emerging companies, belonging to the so-called NewSpace sector [3]-[5].

Among the realm of SAR applications, maritime surveillance is very important for security and safety applications, as well as because of the growing interest for a sustainable exploitation of the sea resources by controlling illegal fishing activities. The capability of detecting ships from traditional SAR systems has been investigated in a number of studies [6]-[20]. Furthermore, some countries like New Zealand are considering the use of dedicated spaceborne SAR systems for the surveillance of their Exclusive Economic Zone [21].

The paper addresses the design of a low-cost SAR for a single, dedicated application, namely ship monitoring, that can be implemented using a small satellite, characterized by low average transmit power and ideally by a small antenna, which is one of the key elements that impact the spacecraft mass and cost [22].

As a consequence of the low transmit power, the system sensitivity, i.e., the noise-equivalent sigma zero (NESZ), will be much worse compared to traditional SAR systems. Moreover, reducing the antenna size will allow improving the azimuth resolution at the expense of a worse NESZ and reduced achievable unambiguous swath.

As for the specific application, it is important to note that ships usually show up in the SAR images as individual pixels or groups of pixels which are very bright compared to their surroundings. Furthermore, azimuth ambiguities of the ships appear in known positions and will be recognized as such rather than considered as distinct ships [23]-[24]. This suggests that one could choose a pulse repetition frequency (PRF) much smaller than the nominal Doppler bandwidth and increase the swath beyond the classical SAR limitation imposed by the resolution, thus guaranteeing a shorter revisit time, from which this application would significantly benefit.

Based on the considerations above, we follow an application-driven design, where the main imaging requirements (NESZ, spatial resolution, and swath width) are determined from the main application requirements, i.e., the minimum size of the ships of interest, the probability of detection (PD), the probability of false alarm (PFA), and the observation frequency, and are used as a starting point for the design of the low-cost SAR system. This approach is sketched in Fig. 1. Here it is important to stress that the severely-increased NESZ level makes the ship detection problem much more challenging and calls for specific considerations and that, due to the use of a PRF much lower than the nominal Doppler bandwidth, the specific SAR system design criteria will differ from those adopted in the conventional case.

The paper is organized as follows. In Section II the minimum NESZ and resolution, required to detect ships of a given minimum size with a desired PD and PFA, are derived in closed form. For their derivation, TerraSAR-X data with ships are exploited to empirically characterize the statistical distribution of the intensity of the pixels occupied by a ship. As a wide imaging swath is another requirement for surveillance applications, the exploitation of a new "ambiguous" SAR concept with a PRF much smaller than the nominal Doppler

bandwidth is discussed in Section III. In Section IV the design principles for such an ambiguous SAR concept and several design examples in X band with small antennas and low average transmit powers are presented. Conclusions are drawn in Section V.

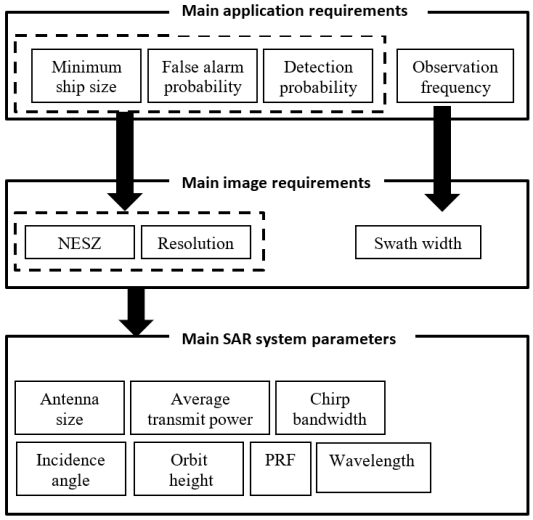

Fig. 1 Application-driven approach for the design of a low-cost SAR for continuous ships monitoring.

II. Image Quality Requirements for Ship Detection

Following the application-driven approach depicted in Fig. 1 as a first step, we present in the following an original derivation of the minimum image quality requirements in terms of NESZ and resolution necessary to ensure the detection of ships of a given minimum size with a desired PD and PFA.

Following the main application requirements, we assume that we want to monitor ships of a given minimum size within a given area of interest. As in [25] we classify ships in three different classes based on their length l: small ships with $l \leq 25$ m, medium ships with $25 < l \leq 150$ m, and large ships with $150 < l \leq 400$ m. It is expected and assumed that for high resolution SAR images characterized by an area of the resolution cell

$$A_{cell} = \delta_a \delta_{r_{gr}} \tag{1}$$

being δ_a the azimuth resolution and $\delta_{r_{gr}}$ the ground-range resolution, the ship will occupy more than one resolution cell. If A_{ship} is the ship area, the number of resolution cells occupied by the ship is given by

$$n_{cell} = A_{ship}/A_{cell} \tag{2}$$

Practical requirements call for very low values of PFA $< 10^{-9}$ [26] with the aim of reducing the costs of the authorities that should identify specific vessels and their activity within the area of interest. The PFA can also be expressed as the number of false alarms per million of km^2. This quantity will be linked to the PFA later on in Section II.C. Regarding the PD, in many situations an effective monitoring of the illegal ships is missing and values of PD in the order of 0.5 are deemed as acceptable, as they would represent a significant improvement with respect to the state of the art [21]. Finally, the required observation frequency will drive the swath width.

The minimum NESZ and resolution necessary for the detection of a ship of a given size also depend on the detection algorithm. We exploit a simple, conservative detection approach that is effective for our noisy scenario and allows deriving the main SAR system parameters. More sophisticated detection algorithms, also including approaches where raw data are processed in a different way, can be of course applied to the acquired data and might further improve the performance.

For the detection problem, we model the complex focused SAR images as the sum of three main signal components: the signal backscattered from the ships, the sea clutter, and the thermal noise. The last two components represent the disturbance.

A. Disturbance and ship characterization

In conventional SAR systems with low values of NESZ (i.e., NESZ ≤ -18 dB) the sea clutter is the dominant component of the disturbance and a number of studies [27]-[29] have been dedicated to model it. In contrast, for systems with low transmit power the thermal noise could become the dominant component. This was shown in [21] by simulation assuming K-distributed sea clutter. We have extracted different patches of sea clutter from single-look TerraSAR-X focused data acquired in both Stripmap (with nominal resolution of 3 m × 3 m) and Spotlight mode (with nominal resolution of 1 m × 2 m) corresponding to different sea state conditions, added white Gaussian noise, and observed that the sea clutter component of the disturbance in most cases can be neglected for NESZ≥ -8 dB. Fig. 2 shows the comparison of the empirical PDF of two different patches before and after adding noise (NESZ=-8 dB), with the corresponding negative exponential distribution of only noise (both axes are displayed in log-scale).

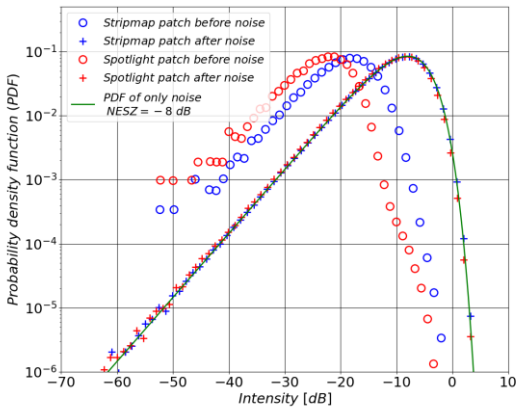

Fig. 2 Comparison of the empirical PDF of two patches of TerraSAR-X data in Stripmap mode (blue markers) and spotlight mode (red markers) before and after adding the noise with the theoretical PDF of only noise (green curve) for a NESZ=-8 dB.

As can be observed, there is a close match between the theoretical PDF of noise and the empirical PDF of the sea clutter data after adding the noise.

Moreover, the distribution can be better characterized by estimating the noise variance from the data rather than using the nominal NESZ.

The next step is the characterization of the ships in single-look focused SAR images, which appear as very bright features because of the effect of multiple corner-reflector-like bounces between the ship and sea and among the ship's metallic structure. Rather than resorting to models, we extract different types of ships from single-look TerraSAR-X images to empirically characterize their intensity distribution. The dataset contains about 500 ships in HH and VV polarizations, with incidence angles ranging from 22° to 40°. The ship class was determined by estimating the ships' length from the images. The same approach can be used to design systems at different wavelengths by using different ship statistics, which can be extracted from data of sensors with the desired wavelength and resolution.

Different distributions were fitted to the intensity data and the lognormal distribution, also in agreement with [21], was shown to provide the best fit:

$$p_I(I) = \frac{1}{I\sqrt{2\pi V}} \exp\left[-\frac{(\ln I - \beta)^2}{2V}\right] \quad (3)$$

where β and V are the mean and the variance of $\ln I$ being $\ln(\cdot)$ the natural logarithm and I the pixel intensity. Fig. 3 shows the empirical PDF of the intensity of ships in Stripmap mode of all the three classes with the corresponding lognormal distribution fitting. In Table 1 the estimated parameters of the log-normal distribution, i.e.,

$$\hat{\beta} = \frac{1}{N}\sum_{i=1}^{N} \ln(I_i)$$
$$\hat{V} = \frac{1}{N}\sum_{i=1}^{N} \ln(I_i)^2 - \left[\frac{1}{N}\sum_{i=1}^{N} \ln(I_i)\right]^2 \quad (4)$$

and the mean value and standard deviation of the ship intensity in dB are reported for all the three ship classes (for the small one the parameters are also provided for very-high resolution spotlight data). As expected, we observe that the mean value and the standard deviation increase moving from small ships to large ships. In particular, small ships have a mean value that is 9 dB smaller than large ships. Moreover, we note that for a fixed wavelength, polarization, and incidence angle the mean value and the standard deviation of the intensity of ships increase moving from low to high resolution.

B. Detection approach

The proposed simple detection approach consists of two main stages as depicted in Fig. 4:

Table 1 Ship parameters for all three ship classes and different acquisition modes/resolutions

Ship class	Mean Value [dB]	Standard deviation [dB]	β	V
Large (Stripmap)	0.63	10.09	0.144	5.40
Medium (Stripmap)	0	9.37	-0.002	4.66
Small (Stripmap)	-8.64	5.30	-1.989	1.490
Small (Spotlight)	-4.03	8.46	-0.928	3.796

- *Stage-1:* A pixel-by-pixel detector is implemented which compares the intensity of the single-look SAR image intensity with a threshold T to detect pixels where a ship can be potentially present. The threshold T is selected to ensure a desired PFA. At the output of this stage a binary image is obtained. Depending on the threshold T, one or more pixels occupied by the ship may exceed the threshold.
- *Stage-2:* All nearby detected pixels by the first stage are clustered together into one detected target through a two-dimensional (2-D) binary integrator that generalizes the standard binary integrator to the 2-D case [30]. The 2-D binary integrator is applied to the binary image at the output of the stage-1 through a 2-D moving window that has the same shape, size, and orientation of the ship, which are assumed to be known. These assumptions will be removed in the following. Finally, a ship is declared as detected, if K ($1 \leq K \leq n_{cell}$) out of n_{cell} pixels occupied by the ship exceed the threshold T.

C. Detection performance and image quality requirements

The detection performance in terms of PFA and PD at the output of two-stage detector can be derived recalling the well-known binomial expression:

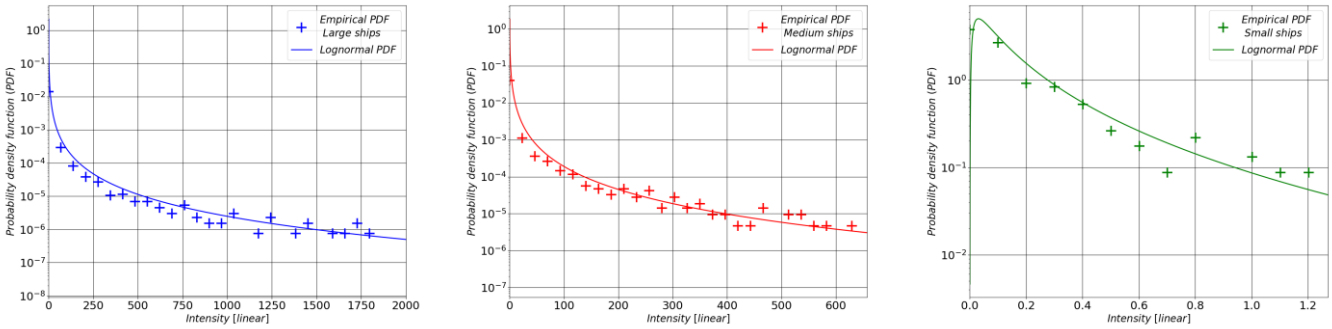

(a) (b) (c)

Fig. 3 Comparison of the empirical PDF of the intensity of the extracted ships from TerraSAR-X data in Stripmap mode and the theoretical lognormal distribution for (a) large ships, (b) medium ships, and (c) small ships.

This article has been accepted for publication in a future issue of this journal, but has not been fully edited. Content may change prior to final publication. Citation information: DOI 10.1109/JSTARS.2021.3136935, IEEE Journal of Selected Topics in Applied Earth Observations and Remote Sensing

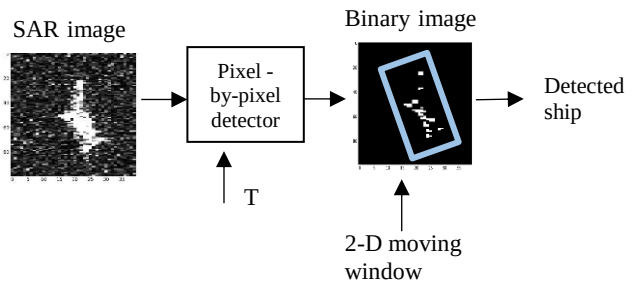

Fig. 4 Block diagram of the ship detection technique.

$$\begin{cases} P_{fa_{ship}} = \sum_{k=K}^{n_{cell}} \binom{n_{cell}}{k} P_{fa_{pixel}}^{k} (1 - P_{fa_{pixel}})^{n_{cell}-k} \\ P_{d_{ship}} = \sum_{k=K}^{n_{cell}} \binom{n_{cell}}{k} P_{d_{pixel}}^{k} (1 - P_{d_{pixel}})^{n_{cell}-k} \end{cases} \quad (5)$$

where $P_{fa_{ship}}$ and $P_{d_{ship}}$ represent the false alarm probability and detection probability of the ship at the output of the 2-D binary integrator, respectively; and $P_{fa_{pixel}}$ and $P_{d_{pixel}}$represent the false alarm probability and the detection probability of the pixel at the output of the pixel-by-pixel detector, respectively. For values of $P_{fa_{ship}} \ll 1$ the expression of $P_{fa_{ship}}$ in (5) can be approximated as:

$$P_{fa_{ship}} \approx \binom{n_{cell}}{K} P_{fa_{pixel}}^{K} \quad (6)$$

Assuming a negative exponential distribution for the background disturbance $P_{fa_{pixel}}$, i.e., the PFA at the output of the first stage, and the detection threshold as function of NESZ are given by:

$$P_{fa_{pixel}} = \exp(-\frac{T}{NESZ}) \quad (7)$$

$$T = -NESZ \ln\left[\binom{n_{cell}}{K}^{-1/K} P_{fa_{ship}}^{1/K}\right] \quad (8)$$

For a fixed $P_{fa_{ship}}$, n_{cell}, and NESZ the threshold T decreases as K increases from 1 to n_{cell}. This means that for K=1 a higher threshold T is set at the first stage.

The probability of detection at the output of the first stage ($P_{d_{pixel}}$) depends on the NESZ and also on the PDF of the ship and is derived as in [31]:

$$P_{d_{pixel}} = \int_0^{\infty} P_{d|A}(x) P_A(x) dx \quad (9)$$

where $P_{d|A}(x)$ denotes the detection probability conditioned over the amplitude random variable, $A = \sqrt{I}$,

$$P_{d|A}(x) = \int_T^{\infty} e^{-|A|^2 NESZ - x} I_0(2A\sqrt{xNESZ}) dx \quad (10)$$

being $I_0(\cdot)$ the modified Bessel function of the first kind and order 0 and $P_A(x)$ denotes the amplitude PDF of the ship which is still a log-normal distribution with $\beta_A = \beta/2$ and $V_A = V/2$.

Once $P_{fa_{pixel}}$ and $P_{d_{pixel}}$ are defined, in order to derive the PFA and PD of the ship in (5) the optimum value of K must be chosen. For a given a n_{cell} occupied by the ship the optimum value of K, K^{opt}, is defined as that K which maximizes the $P_{d_{ship}}$ for a given $P_{fa_{ship}}$ and NESZ. Fig. 5 shows the $P_{d_{ship}}$ as function of NESZ and K for $P_{fa_{ship}} = 10^{-12}$ and a medium ship with $n_{cell} = 106$, that corresponds for example to a 40×8 m ship and $A_{cell} = 3$ m^2. For the derivation of the $P_{d_{ship}}$ the β and V parameter corresponding to medium ships reported in Table 1 are used. Similar results are obtained also for small and large ships and different values of $P_{fa_{ship}}$ and n_{cell}. We observe that for our cases of interest, $K^{opt} = 1$. The value of $K^{opt} = 1$ can be explained by investigating the PDF of the intensity of the background and the PDF of the intensity of the ships. The ship distribution is a lognormal distribution which is part of the family of heavy tailed distribution, whose tails are not exponentially bounded and go down slowly. For SAR systems where the clutter component is not negligible, the disturbance PDF is characterized by a longer tail and the optimum value of K might be greater than one.

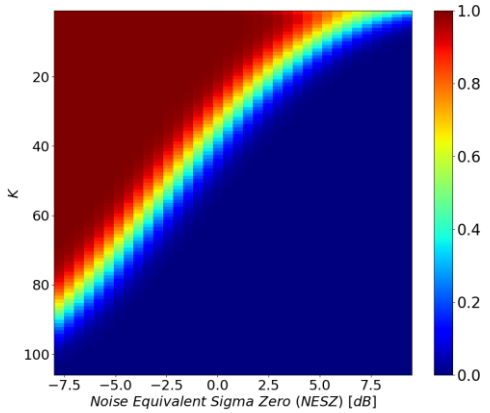

Fig. 5 Probability of detection of the ship, $P_{d_{ship}}$, as function of NESZ and K for a medium ship with $n_{cell} = 106$ and $P_{fa_{ship}} = 10^{-12}$.

$K^{opt} = 1$ implies that the proposed approach simplifies to a single stage, i.e., the first one, and the assumptions of knowing the ship shape, size, and orientation, necessary for the implementation of the second stage, can be removed. To set the threshold T for a specific SAR system characterized by given NESZ and area of the resolution cell, A_{cell}, it is sufficient to know roughly the ship area that we are interested to detect. Substituting in (8) K=1 and (2), we obtain:

$$T = -NESZ \ln\left(\frac{P_{fa_{ship}}}{A_{ship}} A_{cell}\right) \quad (11)$$

The maximum number of ships for a given size of the surveillance area, $A_{surveillance}$, is approximately given as

$$N_{\max ship} \approx A_{surveillance} / A_{ship} \quad (12)$$

This article has been accepted for publication in a future issue of this journal, but has not been fully edited. Content may change prior to final publication. Citation information: DOI 10.1109/JSTARS.2021.3136935, IEEE Journal of Selected Topics in Applied Earth Observations and Remote Sensing

and the following relation between the number of false alarms, $N_{false\ alarms}$, and the $P_{fa_{ship}}$ can be written:

$$N_{false\ alarms} = \frac{A_{surveillance}}{A_{ship}} P_{fa_{ship}} \tag{13}$$

where $P_{fa_{ship}}$ for K=1 is:

$$P_{fa_{ship}}^{K=1} = \frac{A_{ship}}{A_{cell}} P_{fa_{pixel}} \tag{14}$$

As for the detection probability, we can assume that the detected pixel has a very high intensity and the contribution of the noise component in that pixel is negligible. In this case for the computation of the $P_{d_{pixel}}$ in (9) the cumulative distribution function of the log-normal distribution can be used:

$$P_{d_{pixel}}^{K=1} \approx \frac{1}{2} - \frac{1}{2}\mathrm{erf}\left(\frac{\ln T - \beta}{\sqrt{2V}}\right) \tag{15}$$

being erf(·) the error function. Substituting (15) into (5) and after some simple manipulations, the $P_{d_{ship}}$ for $K^{opt} = 1$ can be approximated as:

$$P_{d_{ship}}^{K=1} \approx 1 - \left[\frac{1}{2} + \frac{1}{2}\mathrm{erf}\left(\frac{\ln T - \beta}{\sqrt{2V}}\right)\right]^{\frac{A_{ship}}{A_{cell}}} \tag{16}$$

Finally, based on equations (7), (13), (14), and (16) and after some simple manipulations we derive an approximated closed-form expression of the NESZ as function of the area of the resolution cell, the PD, and the number of false alarms:

$$NESZ \approx -\frac{\exp\left[\sqrt{2V}\,\mathrm{erfinv}\left(2\left(1 - P_{d_{ship}}\right)^{\frac{A_{cell}}{A_{ship}}} - 1\right) + \beta\right]}{\ln\left(\frac{A_{cell}}{A_{surveillance}} N_{false\ alarms}\right)} \tag{17}$$

where erfinv(·) is the inverse error function. This simplified closed-form expression will be exploited in Section IV to design the low-power SAR systems.

Fig. 6 shows the NESZ as function of the resolution cell, A_{cell}, for different values of $P_{d_{ship}}$ and considering a large ship of 300 × 20 m (see continuous curves), a medium ship of 40 × 8 m (see dashed curves) and a small ship of 21 × 6 m (dotted curves) having fixed the number of false alarms per million of km^2 equal to 1 (i.e., $\frac{N_{false\ alarms}}{10^{12} m^2} = 1$). The NESZ in (17) is computed using the lognormal parameters, β and V, of large, medium and small ships reported in Table 1 which refers to the Stripmap mode (resolution $A_{cell} \approx 9$ m^2). As the statistical properties of the ship vary with the resolution and higher values of β and V are expected as the resolution improves, the values of NESZ necessary to guarantee a desired PD for $A_{cell} < 9$ m^2 shown in Fig. 6 are pessimistic compared to the effective values and this in turn will lead to a conservative system design. We observe that for a given ship and fixed number of false alarms, as the resolution cell improves by a factor of two, the same probability of detection is ensured for a NESZ almost 3 dB higher. For example, for the detection of a medium ship in Fig. 6, with $P_{d_{ship}} = 0.9$ for $A_{cell} = 4$ m^2 a $NESZ$ = 3.7 dB is necessary, instead $NESZ$ = 6.2 dB and $NESZ$ = 8.5 dB are sufficient for $A_{cell} = 2$ m^2 and $A_{cell} = 1$ m^2, respectively.

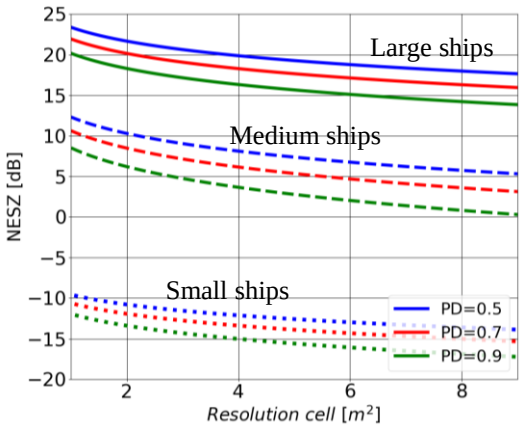

Fig. 6 NESZ as function of area of the resolution cell, A_{cell}, for different values of PD and for a number of false alarms per million of km^2 equal to 1. The continuous curves refer to a large ship with a $A_{ship} = 300 \times 20$ m^2, the dashed curves refer to a medium ship with $A_{ship} = 40 \times 8$ m^2 and the dotted curves refer to a small ship with $A_{ship} = 21 \times 6$ m^2.

We also show two examples to verify the derived detection performance expressions for two ships extracted from TerraSAR-X images, to which noise has been added artificially. Fig. 7 (a) shows a medium ship of 69 m length (image resolution 3 m × 3 m). Noise corresponding to different values of NESZ is added to the image and the intensity is compared to the detection threshold defined as in (11) having fixed $P_{fa_{ship}} = 10^{-10}$. We observe that the ship is detected up to values of $NESZ = 11$ dB, which corresponds to a detection threshold $T =$ 25.52 dB. Fig. 7 (b) shows the same ship as in Fig. 7 (a) after adding noise ($NESZ$ = 11 dB), where the ship structure is not visible anymore. Fig. 7(c) shows the theoretical probability of detection in (16) for the considered case study. We observe that $NESZ$ = 11 dB corresponds to $P_{d_{ship}} = 0.57$. Similar results are reported for a second ship in the Fig. 7 (d) which is a small ship of 21 m length (image resolution 1 m × 2 m). We observed that the ship is detected up to values of $NESZ = 8$ dB which corresponds to a detection threshold $T = 22.52$ dB. Fig. 7(e) shows the same ship after adding noise with $NESZ$ = 8 dB and Fig. 7(f) shows the probability of detection as function of the NESZ. We observe that $NESZ$ = 8 dB corresponds to a $P_{d_{ship}} = 0.15$. In both cases we observe that the critical threshold falls on the knee of the PD vs. NESZ plot.

III. Ambiguous SAR: Wide Swath and High Azimuth Resolution without Digital Beamforming

The design of conventional SAR systems is driven by range and azimuth ambiguities, which arise due to the fact that the,

This article has been accepted for publication in a future issue of this journal, but has not been fully edited. Content may change prior to final publication. Citation information: DOI 10.1109/JSTARS.2021.3136935, IEEE Journal of Selected Topics in Applied Earth Observations and Remote Sensing

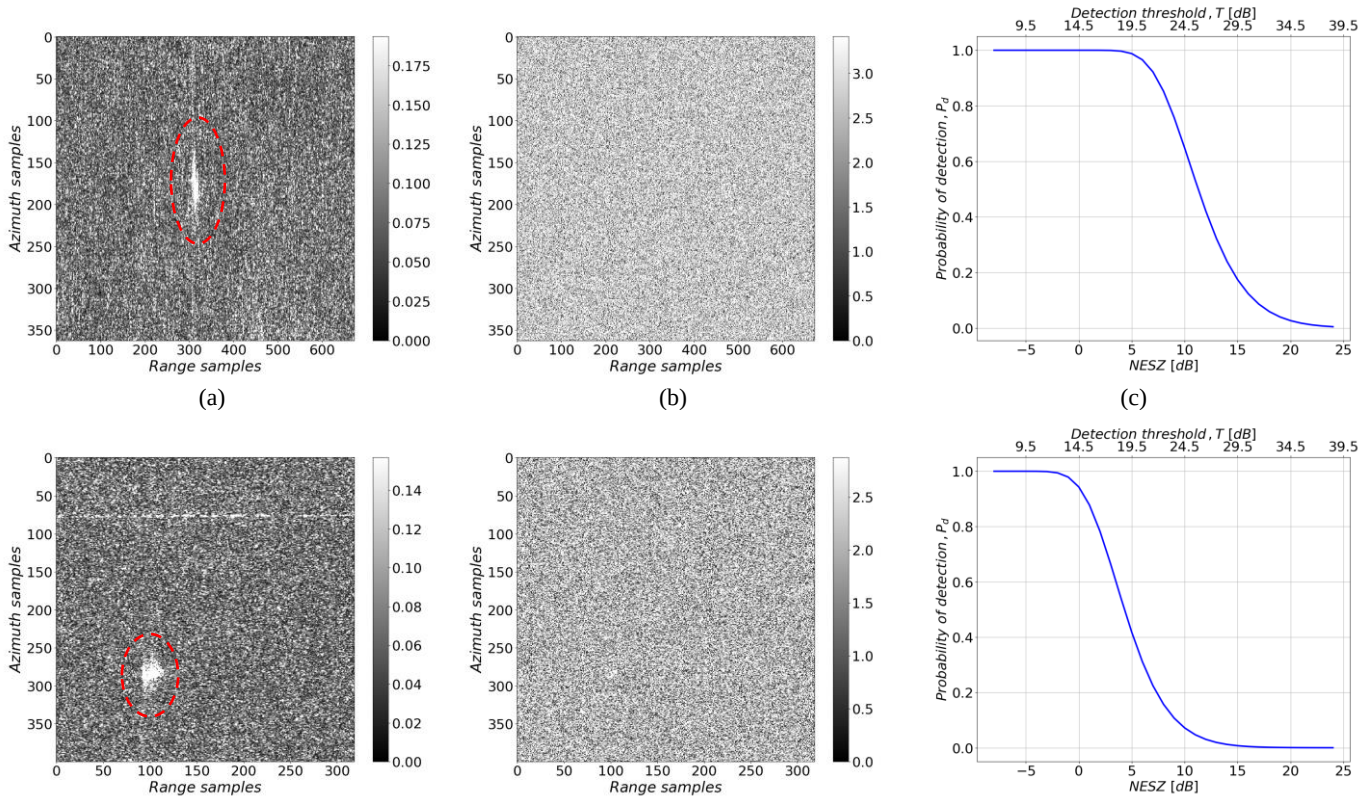

Fig. 7 (a) TerraSAR-X image of a medium ship of 69 m length in Stripmap mode, (b) the corresponding image after adding noise with *NESZ* = 11 dB and (c) the probability of detection of a medium ship as function of the NESZ from a system with $A_{cell} \approx 9$ m^2 and for a $P_{fa_{target}} = 10^{-10}$ (d) TerraSAR-X image of a small ship of 21 m length in spotlight mode, (e) the corresponding image after adding noise with NESZ=8 dB and (f) the probability of detection of a small ship as function of the NESZ from a system with $A_{cell} \approx 1.6$ m^2 and for a $P_{fa_{target}} = 10^{-10}$.

data are sampled at a given PRF [2]. A high PRF leads to stronger range ambiguities and implies a reduction of the achievable unambiguous swath. On the other hand, a low PRF leads to higher azimuth ambiguities, i.e., Doppler frequencies higher than the PRF are folded into the azimuth spectrum. The lower bound of the PRF is classically determined by the nominal Doppler bandwidth, B_d. It is clear that wide swath coverage and high azimuth resolution pose contradicting requirements on the design of spaceborne SAR systems [2]. This motivated the development of different SAR imaging modes with different tradeoffs between the spatial coverage and azimuth resolution, such as ScanSAR [32] or TOPS-SAR [33] which map a wide swath but provide a coarse resolution and Spotlight mode which improves the azimuth resolution at the cost of noncontiguous coverage along the satellite track. In [34] was proposed the use of a PRF smaller than the nominal Doppler bandwidth, B_d, in combination with a reduced processed Doppler bandwidth (and degraded azimuth resolution) and then exploited for smallsat SAR in [22].

Within our system design we exploit a conventional stripmap mode with a PRF much smaller than the nominal Doppler bandwidth to image a wide swath, but differently from [22] and [34] the processed Doppler bandwidth is set equal to B_d in order to have a high azimuth resolution. This is because the azimuth ambiguities of the ships and the increased clutter power (as long as it remains below the noise level) can be tolerated. In this way wide-swath imaging and high azimuth resolution are simultaneously achieved. We name this concept ambiguous SAR. For instance, the TerraSAR-X in Stripmap mode can image a swath width on ground of 30 km and has a nominal azimuth resolution of 3 m. With the ambiguous mode and a PRF that is 3 times smaller than the Doppler bandwidth, we can image a swath width on ground of 90 km, similar to the ScanSAR/TOPS mode (i.e., 100 km), but with an azimuth resolution of 3 m that is 5 times better than that of the ScanSAR/TOPS mode (i.e., 16 m). Fig. 8 compares the ambiguous SAR mode with the Stripmap and ScanSAR/TOPS mode.

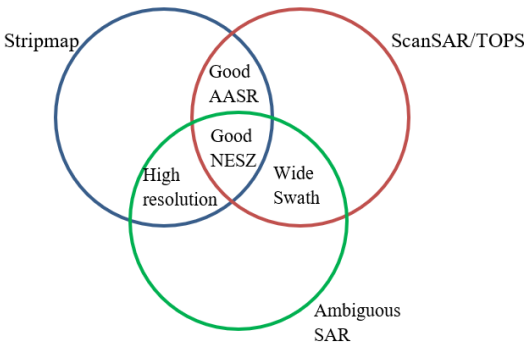

Fig. 8 Comparison of the Stripmap, ScanSAR/TOPS mode with the ambiguous SAR mode.

The possibility of achieving wide swaths at the expense of azimuth ambiguities had been already proposed by NovaSAR and implemented as its "maritime mode" [23] - [24], [35] - [36]. This mode, however, is based on the ScanSAR acquisition mode with six sub-swaths, is characterized by a resolution of 13.7 m × 6 m, and allows detecting medium ships with a false alarm rate of 10^{-7} [36].

High resolution and wide swath can also be obtained using digital beamforming techniques [37]-[39], which also guarantee a low azimuth ambiguity-to-signal ratio (AASR), but at the expense of higher costs and greater system complexity.

Why ambiguities can be tolerated for this specific application?

The azimuth ambiguous signals are displaced in azimuth, since they are generated during the illumination intervals preceding and succeeding the illumination time of the main signal. As the positions of the ambiguities are known, even if a strong azimuth ambiguity exceeds the threshold, it will be recognized as such and not considered as a distinct ship. We assume, in fact, that the scenario is sparse and it is unlikely that a ship superimposes to the ambiguities of another ship.

Moreover, the azimuth ambiguities of ships after focusing will be smeared in azimuth and range [40]. This implies a decrease in the peak level for the ambiguities. Therefore, after comparing the SAR image with the threshold *T*, they are not expected to exceed the threshold. Fig. 9 shows a large ship of 260 m length and its azimuth ambiguities for an X-band SAR system with antenna length of 2 m at an orbital altitude of 500 km that has a resolution cell A_{cell} ≈1.6 m^2 (similar to that of the TerraSAR-X images in Spotlight mode) and PRF=1686 Hz (i.e., four times smaller than the nominal Doppler bandwidth B_d = 6744 Hz). We note that the azimuth ambiguities are visible but nevertheless the maximum peak value of the first ambiguities is 14 dB below the maximum peak value of the main signal.

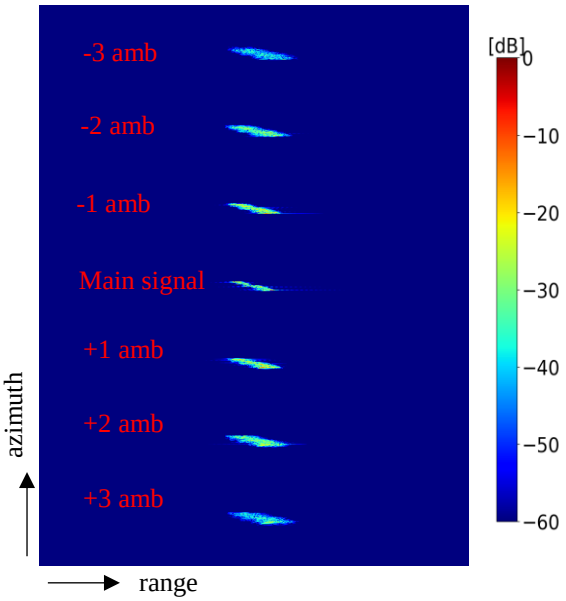

Fig. 9 Ship of 260 m length and its azimuth ambiguities for an X-band system with a PRF four times smaller than the nominal Doppler bandwidth.

For small ships, for which a detection of the main signal is critical, the ambiguities are therefore likely to be well below the noise level.

Another aspect to account for when choosing a PRF much smaller than the nominal Doppler bandwidth is that the clutter will backfold as well, contributing to a significant increase of its energy, with AASR > 1 or 0 dB. Having fixed the processed Doppler bandwidth B_p equal to the nominal Doppler bandwidth B_d, i.e., $B_p = B_d$, the AASR will increase as the PRF decreases. The AASR as function of $M = \frac{B_d}{PRF}$ for $M \geq 2$ can be approximately fitted by the following expression:

$$AASR \approx -0.98 + 0.75M \tag{18}$$

Fig. 10 compares the AASR as function of M with the approximated expression in (18) and a good agreement is observed validating the above closed form expression.

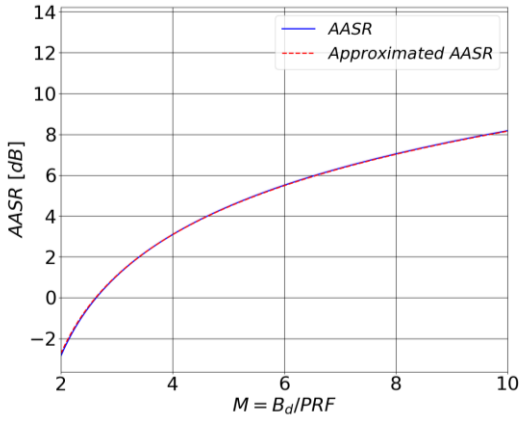

Fig. 10 Comparison of the azimuth ambiguity-to-signal ratio with the approximated expression of AASR in equation (18) as function of M having set the processed Doppler bandwidth equal to B_d.

Always under the assumption $M \geq 2$ the clutter-to-noise ratio of the ambiguous SAR can be therefore expressed as:

$$CNR_{amb} = (AASR + 1)\, CNR \approx 0.75M \cdot CNR \tag{19}$$

where CNR is the clutter-to-noise ratio of the non-ambiguous SAR and the expression in (18) has been used.

As the sea clutter component is the sum of one unambiguous and M ambiguous components and the latter components are also "smeared", it is likely to be characterized by a distribution with a tail that goes down faster compared to that of the non-ambiguous SAR.

Selecting a PRF M times smaller than B_d will allow imaging a swath that is approximately M times wider. Nevertheless, the PRF cannot be arbitrarily small because the wider the swath to be imaged, the greater the power to be transmitted and our system is power limited.

Once the range of selectable PRFs is defined from the swath width requirement, the exact PRF value will be chosen using the timing diagram in order to avoid blind ranges, due to the fact that the radar cannot receive while it is transmitting, and the returns from nadir [2]. To relax even more the constrains on

the selection of the PRF, we can get rid of the nadir echo return by exploiting the waveform-encoded SAR concept, i.e., alternating, e.g., up- and down- chirps on transmit and remove the nadir echo within a postprocessing step [41]-[42].

How to get a high azimuth resolution?

The received raw data are sampled in azimuth direction by a PRF that is *M* times smaller than B_d and after accomplishing the range compression and the range cell migration correction, in order to focus the data along azimuth direction with the highest azimuth resolution, i.e., the one given by the antenna length/nominal Doppler bandwidth, a zero padding of the data along azimuth can be done by adding between each consecutive range line *M* range lines of zeros before convolving it with the azimuth filter of a system with a PRF *M* times higher.

For a system with a PRF much smaller than the nominal Doppler bandwidth, azimuth ambiguities do not originate from the sidelobes of the azimuth antenna pattern, but from its main lobe. By processing the full nominal Doppler bandwidth as explained above, we therefore exploit through coherent integration the energy of *M* orders of azimuth ambiguities to achieve high azimuth resolution.

IV. System Design

Once the image requirements, i.e., NESZ, resolution, and swath width, have been derived from the application requirements we need to choose the system parameters of our SAR. In this section we present the specific SAR system design criteria for a system operated in "ambiguous" mode, which differ from those adopted in the conventional case.

Following the discussion in Section II, where we noted that we can roughly trade 3 dB of spatial resolution with 3 dB of NESZ, (17) can be rewritten by multiplying NESZ on the left by A_{cell} and dividing A_{cell} on the right by A_{cell} as:

$$NESZ \cdot A_{cell} \approx -\frac{\exp\left[\sqrt{2V}\,\mathrm{erfinv}\left(2\left(1-P_{d_{ship}}\right)^{\frac{1}{A_{ship}}}-1\right)+\beta\right]}{\ln\left(\frac{N_{false\ alarms}}{A_{surveillance}}\right)} \tag{20}$$

obtaining an expression where the product of the image quality requirements, $NESZ \cdot A_{cell}$ depends on the detection performance and ship size.

We can then recall the well-known expression of the NESZ of a SAR for a distributed target (the ship is considered as a distributed target, as we assume that it occupies several resolution cells):

$$NESZ = \frac{4^4\,\pi^3\,R_0^3\,B_r \sin\theta_i\,v_s\,k\,T_s\,L_{az}\,F\,L_{sys}}{P_{avg}\,G^2\,\lambda^3\,c} \tag{21}$$

where R_0 is the slant range, B_r is the chirp bandwidth, θ_i is the incidence angle, v_s is the satellite velocity, k is the Boltzman constant, T_s is the system temperature, L_{az} is the azimuth losses, $F \cdot L_{sys}$ is the loss factor that includes all other losses (atmospheric, system, etc.) and the noise figure, P_{avg} is the average transmit power, G is the Tx-Rx antenna gain, λ is the wavelength and *c* is the speed of light. For a processed Doppler bandwidth equal to the nominal Doppler bandwidth $L_{az} = 1.3$ dB.

Substituting in (21) the expression of the antenna gain as a function of the antenna size for a rectangular antenna:

$$G = \frac{4\pi}{\lambda^2}\eta\,L_a W_a \tag{22}$$

where L_a is the antenna length, W_a is the antenna height and η is the antenna efficiency and using the definition of the swath width in ground, W_g:

$$W_g = \frac{\lambda R_0}{W_a \cos\theta_i} \tag{23}$$

the expression of NESZ in (21) can be written as:

$$\frac{NESZ \cdot A_{cell}}{{W_g}^2} = \frac{4\,\pi\,R_0 \cos^2\theta_i\,v_s\,k\,T_s\,L_{az}\,F\,L_{sys}\,L_{pattern}}{P_{avg}\,L_a\,\lambda\,\eta^2} \tag{24}$$

where we have further introduced a term $L_{pattern}$ which takes into account the NESZ variation between the swath center and far range due to the antenna elevation pattern, the slant range and incidence angle. This is because we want to guarantee the detection of the ships with the desired performance over the whole swath. This implies that better detection performance will be obtained at the swath center. From (24) we can obtain the pair of P_{avg} and L_a which guarantee the desired image requirements on the left side of the equation.

The antenna height, W_a, and the maximum value of PRF, PRF_{max} are driven by the value of the ground swath W_g:

$$W_a = \frac{\lambda R_0}{W_g \cos\theta_i} \tag{25}$$

$$PRF_{max} = \frac{c}{2W_g \sin\theta_i}(1-2D) \tag{26}$$

where *D* is the duty cycle and the factor 2 considers pulse compression.

Once we have selected the antenna length, the nominal Doppler bandwidth of the system is defined and the value of *M* is given by:

$$M = \frac{B_d}{PRF_{max}} \tag{27}$$

One can notice from (24) that the chirp bandwidth does not influence the performance. This is due to the fact that the performance approximately depends on the product of spatial resolution and NESZ and the chirp bandwidth is inversely proportional to the range resolution and directly proportional to the NESZ. A smaller chirp bandwidth allows reducing the data rate, which might be critical for a low-cost system with high azimuth resolution and wide swath. However, the overall

assumption for the system requires that the resolution is much smaller than the ship size and the resolution further influences the statistical parameters of the ship, as mentioned in Section II. A very high resolution leads to more favorable statistics and is therefore the key to detect very small ships.

In the following, five different examples of X-band systems exploiting the ambiguous SAR concept are presented. Table 2 collects for each of the five scenarios and systems the application requirements, the main imaging requirements, and the main SAR system parameters. For all the considered scenarios we select an orbit height of 500 km, an incidence angle $\theta_i = 30°$, a chirp bandwidth $B_r = 300$ MHz and a duty cycle of 10%. We also assume $L_{az} = 1.3$ dB and $F \cdot L_{sys} = 5$ dB.

For the scenario A we are interested to detect medium ships (40 m × 8 m) with a $P_{d_{target}} = 0.5$ and $\frac{N_{false\ alarms}}{10^{12}\mathrm{m}^2} = 1$ over a ground swath $W_g = 90$ km. To image a 90-km ground swath an antenna height $W_a = 0.22$ m is needed at X band and the upper bound on the PRF to receive the full echo from the swath is $PRF_{max} = 2665$ Hz. Based on (20) the product of the image quality parameters, $NESZ \cdot A_{cell}$, is computed using the β and V parameter of medium ships in Stripmap mode reported in Table 1. From (24) different pairs of P_{avg} and L_a are computed, which satisfy the image requirements. In (24) $L_{pattern}$ for the considered scenarios is assumed equal to 6 dB. For this scenario we select an antenna length $L_a = 1$ m and $P_{avg} = 46$ W. From the antenna length the nominal Doppler bandwidth and the azimuth resolution are obtained as $B_d = 13489$ Hz and $\delta_a = 0.5$ m, respectively. For this case, the PRF_{max} is $M = 5$ times smaller than B_d. Now that the $A_{cell} = 0.5$ m^2 is defined, from the product $NESZ \cdot A_{cell}$ we derive the NESZ which is 15.3 dB. One can note that the NESZ is much greater than -8 dB and the clutter contribution, following the discussion in Section II, can be considered negligible with respect to the thermal noise. From the timing diagram the exact value of the PRF is selected.

For the scenario B we are interested to detect again medium ships with the same detection performance as in scenario A but we want to image a smaller swath, i.e., 60 km. Based on (25) and (26) we need a $W_a = 0.33$ m to image 60 km swath in ground and $PRF_{max} = 4000$ Hz. As before after deriving the product of $NESZ \cdot A_{cell}$ we select the pair of P_{avg} and L_a that ensures the desired requirements. For this scenario we select the same antenna length of $L_a = 1$ m and as the swath width that we want to image is smaller we need a $P_{avg} = 20$ W. For this scenario we have the same $A_{cell} = 0.5$ m^2 and $NESZ = 15.3$ dB as for the scenario A. Instead the PRF_{max} is 3.4 times smaller than B_d.

For the scenario C we are interested in the detection of small ships (21 m × 6 m) with the same detection performance as in scenario B and same swath width in ground of 60 km. The antenna height and the PRF_{max} are the same as for the scenario B. As before we firstly compute the $NESZ \cdot A_{cell}$ using the β and V parameter of small ships obtained from Spotlight data reported in Table 1. For this scenario we select then a longer antenna of 2.5 m and $P_{avg} = 68$ W to guarantee the desired requirements. We note that because we want to detect a small ship a greater P_{avg} and a longer antenna is need to have the same detection performance and image the same swath as for the medium ships of scenario B. For this scenario we have an $A_{cell} = 1.25$ m^2 and $NESZ = 2.1$ dB. Instead the PRF_{max} is 1.3 times smaller than $B_d = 5395$ Hz.

Scenario D is similar to the previous scenario but the detection probability is set equal to 0.4, i.e., smaller compared to the previous case. For this scenario we use a shorter antenna of 1.8 m and $P_{avg} = 77$ W. Because of the lower probability of detection we have almost the same P_{avg} as for the previous case but using a shorter antenna. In this case we get $A_{cell} = 0.9$ m^2, a $NESZ = 4.4$ dB and a PRF_{max} that is 1.8 times smaller than $B_d = 7494$ Hz.

In the scenario E we are interested to detect even smaller ships of 16 m × 5 m size with the same detection performance as in scenario D and image a smaller swath in ground of 50 km. Following the same strategy, for this case we have an antenna height of 0.39 m and a $PRF_{max} = 4800$ Hz. Afterwards we select for this scenario the same antenna length as for D, $L_a = 1.8$ m and $P_{avg} = 72.2$ W. Almost the same average transmit power is need in this case compared to the scenario C, even though we want to detect a smaller ship. This is because we image a swath width in ground 16% smaller. In this case we have an $A_{cell} = 0.9$ m^2, a $NESZ = 2.6$ dB and a PRF_{max} that is 1.4 times smaller than B_d.

These design examples show that is possible to detect small ships (i.e., size 21 m × 6 m or even 16 m × 5 m) with small antenna length in the order of 1-2.5 m by transmitting an average transmit power lower than 80 W, i.e., at least one order of magnitude smaller than conventional SAR systems such as TerraSAR-X or even microsatellite SAR, such as ICEYE's ones, if one also considers that for our design examples the swath is wider [5].

It is important to remember that the required probability of detection (see Minimum Probability of detection in Table 2) is guaranteed at the near and far range of the swath. Because of the 6 dB variation of NESZ between the swath center and far range we ensure for all the case studies a probability of detection at mid swath greater than 0.95 (see Maximum Probability of detection in Table 2).

In addition, the maximum and the minimum probability of detection refer to the given ship size for each considered scenario. This means that ships of greater dimensions will be detected with a better probability of detection for the same number of false alarms.

The proposed concept could exploit an additional polarization (dual-pol) to improve the detection performance [43] - [50]. The improved performance, however, comes at the expense of an increased complexity and cost. In particular, the data volume to be downlinked, already intrinsically huge due to the high resolution and the wide imaged swath, would increase by a factor of two.

A further issue is, even for single-pol systems, the selection of the optimal polarization on both transmit and receive that maximizes the detection performance. This could be derived from existing data and depends on the wavelength and the incidence angle.

Table 2 System design examples in X band operating in ambiguous mode

Application requirements						
Ship size	A_{target}	Scenario A 320 m^2 (40 m × 8 m)	Scenario B 320 m^2 (40 m × 8 m)	Scenario C 126 m^2 (21 m × 6 m)	Scenario D 126 m^2 (21 m × 6 m)	Scenario E 80 m^2 (16 m × 5 m)
Number of false alarms per million km^2	$\frac{N_{false\ alarms}}{10^{12}\mathrm{m}^2}$	1	1	1	1	1
Minimum probability of detection	P_d	0.5	0.5	0.5	0.4	0.4
Maximum probability of detection (for the below system parameters)	P_d^{max}	0.9868	0.9868	0.9859	0.9649	0.9524
Main imaging requirements						
Noise Equivalent Sigma Zero	*NESZ*	15.3 dB	15.3 dB	2.1 dB	4.4 dB	2.6 dB
Ground range resolution	δ_{rg}	1 m	1 m	1 m	1 m	1 m
Azimuth resolution	δ_a	0.5 m	0.5 m	1.25 m	0.9 m	0.9 m
Swath width in ground	W_g	90 km	60 km	60 km	60 km	50 km
System parameters						
Orbit height	h	500 km				
Incidence angle	θ_i	30°				
Wavelength	λ	0.03 m				
Chirp bandwidth	B_r	300 MHz				
PRF	*PRF*	2442 Hz-2665 Hz	3762 Hz-4000 Hz	3762 Hz-4000 Hz	3762 Hz-4000 Hz	4620 Hz-4800 Hz
Antenna length	L_a	1 m	1 m	2.5 m	1.8 m	1.8 m
Antenna height	W_a	0.22 m	0.33 m	0.33 m	0.33 m	0.39 m
Average transmit power	P_{avg}	46 W	20 W	68 W	77 W	72.2 W

V. Conclusions and Outlook

An application-driven approach for the design of a low-cost SAR that can be implemented on small satellites and dedicated to the ship monitoring application has been presented.

The proposed approach relies on two key insights. The first is the use of a small antenna that can fit in a small satellite and transmits a very low power. For this reason, we derived an original, approximated closed-form expression that relates the NESZ and resolution to the desired detection performance based on ship statistics extracted from TerraSAR-X data. The second insight is the use of an ambiguous SAR mode with a PRF lower than the nominal Doppler bandwidth, ensuring simultaneously wide-swath SAR imaging and high azimuth resolution and tolerating azimuth ambiguities.

From the examples in this paper, it has become clear that using the ambiguous mode it is possible to detect small ships by imaging a wide swath in the order of 60 km and transmitting an

average power lower than 80 W with a small antenna of 1-2.5 m length.

These very-low-power SAR systems can be very effective in detecting illegal (non-cooperating) fishing vessels. In order to distinguish them from cooperating ships, the satellite should be equipped with an automatic identification system (AIS) [24]. From the combination of SAR and AIS data it is possible to identify the illegal vessels and handle this information to the authorities.

The ambiguous SAR mode could be in principle adapted to existing, planned and future SAR systems to have an additional mode for efficient ship detection over ultra-wide swaths. Compared to the design of a smallsat, the latter systems can benefit of a much higher average transmit power, while high azimuth resolution and wide swath can be obtained in systems with larger antennas using tapering [51].

ACKNOWLEDGMENT

The authors would like to acknowledge Mr. Jan Krecke of the University of Auckland, New Zealand, for many constructive discussions and the anonymous reviewers for their helpful comments.

REFERENCES

[1] A. Moreira, P. Prats-Iraola, M. Younis, G. Krieger, I. Hajnsek, and K.P. Papathanassiou, “A Tutorial on Synthetic Aperture Radar,” IEEE Geosci. Remote Sens. Mag., vol. 1, no. 1, pp. 6–43, Jan. 2013.

[2] J. C. Curlander and R. N. McDonough (1991),“Synthetic Aperture Radar systems and Signal Processing” Wiley series in remote sensing.

[3] D. Werner, “A New Hope for Commercial Space-based Radar”, Space News Magazine, March 28, 2016.

[4] D. Castelletti, G. Farquharson, C. Stringham and D. Eddy, “Operational readiness of the Capella Space SAR system,” IGARSS 2020 - 2020 IEEE International Geoscience and Remote Sensing Symposium, Hawaii,2020.

[5] V. Ignatenko, P. Laurila, A. Radius, L. Lamentowski, O. Antropov, D. Muff, “ICEYE microsatellite SAR constellation status update: evaluation of first commercial imaging modes,” IGARSS 2020 - 2020 IEEE International Geoscience and Remote Sensing Symposium, Hawaii,2020.

[6] K. Eldhuset, “An automatic ship and ship wake detection system for spaceborne SAR images in coastal regions,” IEEE Transactions on Geoscience and Remote Sensing, vol. 34, no. 4, pp. 1010–1019, 1996.

[7] P. W. Vachon, J. Campbell, C. Bjerkelund, F. Dobson, and M. Rey, “Ship detection by the RADARSAT SAR: Validation of detection model predictions,” Canadian Journal of Remote Sensing, vol. 23, no. 1, pp. 48–59, 1997.

[8] S. Brusch, S. Lehner, T. Fritz, M. Soccorsi, A. Soloviev, and B. van Schie, “Ship surveillance with TerraSAR-X,” IEEE Transactions on Geoscience and Remote Sensing, vol. 49, no. 3, pp. 1092–1103, Mar. 2001.

[9] D. Crisp, “The state-of-the-art in ship detection in synthetic aperture radar imagery,” Defence Sci. Technol. Org., Port Wakefield, South Australia, Research Report DSTO-RR-0272, Tech. Rep., 2004.

[10] P. Lombardo and M. Sciotti, (2001). Segmentation-based technique for ship detection in SAR images. Radar, Sonar and Navigation, IEE Proceedings.

[11] D. Pastina, F. Fico and P. Lombardo, "Detection of ship targets in COSMO-SkyMed SAR images," 2011 IEEE RadarCon (RADAR), 2011, pp. 928-933.

[12] M. Martorella, F. Berizzi, D. Pastina and P. Lombardo, "Exploitation of Cosmo SkyMed SAR images for maritime traffic surveillance," 2011 IEEE RadarCon (RADAR), 2011, pp. 113-117.

[13] H. Greidanus et al., The SUMO Ship Detector Algorithm for Satellite Radar Images. Remote Sens. 2017, 9, 246.

[14] Qingshan Jiang et al., "Ship detection in RADARSAT SAR imagery," SMC'98 Conference Proceedings. 1998 IEEE International Conference on Systems, Man, and Cybernetics (Cat. No.98CH36218), 1998, pp. 4562-4566 vol.5.

[15] P. Iervolino and R. Guida, "A Novel Ship Detector Based on the Generalized-Likelihood Ratio Test for SAR Imagery," in IEEE Journal of Selected Topics in Applied Earth Observations and Remote Sensing, vol. 10, no. 8, pp. 3616-3630, Aug. 2017.

[16] M. Liao, C. Wang, Y. Wang and L. Jiang, "Using SAR Images to Detect Ships From Sea Clutter," in IEEE Geoscience and Remote Sensing Letters, vol. 5, no. 2, pp. 194-198, April 2008.

[17] C. Bentes, D. Velotto and S. Lehner, "Analysis of ship size detectability over different TerraSAR-X modes," 2014 IEEE Geoscience and Remote Sensing Symposium, 2014, pp. 5137-5140.

[18] P. W. Vachon, J. Wolfe and H. Greidanus, "Analysis of Sentinel-1 marine applications potential," 2012 IEEE International Geoscience and Remote Sensing Symposium, 2012, pp. 1734-1737.

[19] H. Greidanus et al., "Benchmarking operational SAR ship detection," IGARSS 2004. 2004 IEEE International Geoscience and Remote Sensing Symposium, 2004, pp. 4215-4218 vol.6.

[20] C. H. Gierull and I. Sikaneta, "A Compound-Plus-Noise Model for Improved Vessel Detection in Non-Gaussian SAR Imagery," in IEEE Transactions on Geoscience and Remote Sensing, vol. 56, no. 3, pp. 1444-1453, March 2018.

[21] J. Krecke, M. Villano, N. Ustalli, A. C. M. Austin, J. E. Cater and G. Krieger, "Detecting Ships in the New Zealand Exclusive Economic Zone: Requirements for a Dedicated SmallSat SAR Mission," in IEEE Journal of Selected Topics in Applied Earth Observations and Remote Sensing, vol. 14, pp. 3162-3169, 2021.

[22] A. Freeman, “Design principles for smallsat SARs,” in 32nd Annual AIAA/USU Conference on Small Satellites, 2018, Logan, UT, 2018.

[23] P. Iervolino, M. Cohen, R. Guida and P. Whittaker, "Ship-detection in SAR imagery using Low Pulse Repetition Frequency Radar," EUSAR 2014; 10th European Conference on Synthetic Aperture Radar, 2014, pp. 1-4.

[24] P. Whittaker, S. Doodyb, M. Cohenb, B. Schwarza, G. Burbidgeb, R. Birda, "NovaSAR-1 – Early Mission Achievements," EUSAR 2021; 13th European Conference on Synthetic Aperture Radar, 2021, pp. 1-4.

[25] B. Tings, C. Bentes, D. Velotto, et al., “Modelling ship detectability depending on TerraSAR-X-derived metocean parameters,”CEAS Space J 11, 81–94 (2019).

[26] C. H. Gierull and I. Sikaneta, "Potential marine moving target indication (MMTI) performance of the RADARSAT constellation mission (RCM)," EUSAR 2012; 9th European Conference on Synthetic Aperture Radar, 2012, pp. 404-407.

[27] D. J. Crisp, L. Rosenberg, N. J. Stacy and Y. Dong, "Modelling X-band sea clutter with the K-distribution: Shape parameter variation," 2009 International Radar Conference "Surveillance for a Safer World" (RADAR 2009), 2009, pp. 1-6.

[28] S. Angelliaume; L. Rosenberg, M. Ritchie, Modeling the Amplitude Distribution of Radar Sea Clutter. Remote Sens. 2019, 11, 319.

[29] A. Fiche, S. Angelliaume, L. Rosenberg and A. Khenchaf, "Analysis of X-Band SAR Sea-Clutter Distributions at Different Grazing Angles," in IEEE Transactions on Geoscience and Remote Sensing, vol. 53, no. 8, pp. 4650-4660, Aug. 2015.

[30] M.A. Weiner, "Binary integration of fluctuating targets," in IEEE Transactions on Aerospace and Electronic Systems, vol. 27, no. 1, pp. 11-17, Jan. 1991.

[31] G. R. Heidbreder and R. L. Mitchell, "Detection Probabilities for Log-Normally Distributed Signals," in IEEE Transactions on Aerospace and Electronic Systems, vol. AES-3, no. 1, pp. 5-13, Jan. 1967.

[32] K. Tomiyasu, "Conceptual Performance of a Satellite Borne, Wide Swath Synthetic Aperture Radar," in IEEE Transactions on Geoscience and Remote Sensing, vol. GE-19, no. 2, pp. 108-116, April 1981.

[33] F. De Zan and A. Monti Guarnieri, "TOPSAR: Terrain Observation by Progressive Scans," in IEEE Transactions on Geoscience and Remote Sensing, vol. 44, no. 9, pp. 2352-2360, Sept. 2006.

[34] A. Freeman, W. T. K. Johnson, B. Huneycutt, R. Jordan, S. Hensley, P. Siqueira, and J. Curlander, “The "Myth" of the minimum SAR antenna area constraint,” in IEEE Transactions on Geoscience and Remote Sensing, vol. 38, no. 1, p20-324, Jan. 2000.

[35] J. Márquez-Martínez, M. Cohen, S. Doody, P. Lau-Semedo and A. Larkins, "Next generation low cost SAR payloads: Novasar-S and beyond," 2017 IEEE International Geoscience and Remote Sensing Symposium (IGARSS), 2017, pp. 3848-3851.

[36] M. Cohen, A. Larkins, P. L. Semedo and G. Burbidge, "NovaSAR-S low cost spaceborne SAR payload design, development and deployment of a new benchmark in spaceborne radar," 2017 IEEE Radar Conference (RadarConf), 2017, pp. 0903-0907.

[37] N. Goodman, D. Rajakrishna and J. Stiles, "Wide swath, high resolution SAR using multiple receive apertures," IEEE 1999 International Geoscience and Remote Sensing Symposium. IGARSS'99 (Cat. No.99CH36293), 1999, pp. 1767-1769 vol.3.

[38] N. Gebert, G. Krieger and A. Moreira, "Digital Beamforming for HRWS-SAR Imaging: System Design, Performance and Optimization Strategies," 2006 IEEE International Symposium on Geoscience and Remote Sensing, 2006, pp. 1836-1839.

[39] G. Krieger, N. Gebert and A. Moreira, "Unambiguous SAR signal reconstruction from nonuniform displaced phase center sampling," in IEEE Geoscience and Remote Sensing Letters, vol. 1, no. 4, pp. 260-264, Oct. 2004.

[40] F.K. Li and W.T.K. Johnson, “Ambiguities in spaceborne synthetic aperture radar systems,” IEEE Trans. Aerosp. Electron. Syst., vol. 19, no. 3, pp. 389–397, May 1983.

[41] M. Villano, G. Krieger, and A. Moreira, “Nadir Echo Removal in Synthetic Aperture Radar via Waveform Diversity and Dual-Focus Post-Processing,” IEEE Geoscience and Remote Sensing Letters, vol. 15, no. 5, pp. 719-723, May 2018.

[42] S.-Y. Jeon, M. Villano, T. Kraus, U. Steinbrecher, and G. Krieger, “Experimental Demonstration of Nadir Echo Removal in SAR Using Waveform Diversity and Dual-Focus Postprocessing,” IEEE Geoscience and Remote Sensing Letters, online available.

[43] R. Touzi. On the use of polarimetric SAR data for ship detection. In IEEE 1999 International Geoscience and Remote Sensing Symposium (IGARSS'99), volume 2, pages 812-14, 1999.

[44] M. Yeremy, J.W.M. Campbell, K. Mattar, and T. Potter. Ocean surveillance with polarimetric SAR. Canadian Journal of Remote Sensing, 27(4):328-344, 2001.

[45] M. Sciotti, D. Pastina, and P. Lombardo. “Exploiting the polarimetric information for the detection of ship targets in non-homogeneous SAR images,” In IEEE 2002 International Geoscience and Remote Sensing Symposium (IGARSS'02), volume 3, pages 1911-13, 2002.

[46] Han Zhaoying and Chong Jinsong, “A review of ship detection algorithms in polarimetric SAR images,” Proceedings 7th International Conference on Signal Processing, 2004. Proceedings. ICSP '04. 2004., 2004, pp. 2155-2158 vol.3

[47] F. Nunziata, M. Migliaccio and C. E. Brown, “Reflection Symmetry for Polarimetric Observation of Man-Made Metallic Targets at Sea,” in IEEE Journal of Oceanic Engineering, vol. 37, no. 3, pp. 384-394, July 2012.

[48] F. Nunziata and M. Migliaccio, "On the COSMO-SkyMed PingPong Mode to Observe Metallic Targets at Sea," in IEEE Journal of Oceanic Engineering, vol. 38, no. 1, pp. 71-79, Jan. 2013.

[49] D. Velotto, F. Nunziata, M. Migliaccio and S. Lehner, “Dual-Polarimetric TerraSAR-X SAR Data for Target at Sea Observation,” in IEEE Geoscience and Remote Sensing Letters, vol. 10, no. 5, pp. 1114-1118, Sept. 2013.

[50] T. Zhang, A. Marino, F. Nunziata, et al., “Marine target detection using dual-polarimetric SAR imagery,” Journal of Geodesy and Geoinformation Science, 2021.

[51] M. Villano, G. Krieger, A. Moreira, “Advanced Spaceborne SAR Systems with Planar Antenna,” 2017 IEEE Radar Conference, Seattle, WA, USA, 8-12 May 2017.